nature nanotechnology

Article

https://doi.org/10.1038/s41565-023-01320-7

Far-field coupling between moiré photonic lattices

Received: 23 June 2022

Accepted: 9 January 2023

Published online: 13 February 2023

Check for updates

Jun Guan [1] ✉, Jingtian Hu[1], Yi Wang[2], Max J. H. Tan[1], George C. Schatz [1,2] & Teri W. Odom [1,2,3] ✉

Superposing two or more periodic structures to form moiré patterns is emerging as a promising platform to confine and manipulate light. However, moiré-facilitated interactions and phenomena have been constrained to the vicinity of moiré lattices. Here we report on the observation of ultralong-range coupling between photonic lattices in bilayer and multilayer moiré architectures mediated by dark surface lattice resonances in the vertical direction. We show that two-dimensional plasmonic nanoparticle lattices enable twist-angle-controlled directional lasing emission, even when the lattices are spatially separated by distances exceeding three orders of magnitude of lattice periodicity. Our discovery of far-field interlattice coupling opens the possibility of using the out-of-plane dimension for optical manipulation on the nanoscale and microscale.

Moiré lattices—two or more periodic structures stacked with relative twist angles—have enabled unusual phenomena in two-dimensional (2D) materials and structures[1–3]. For example, magic-angle bilayer graphene can facilitate unconventional superconductivity[4–6], anomalous quantum Hall effects[7] and ferromagnetism[8]. Twisted α-MoO_3 bilayers show tunable topological phonon transitions from hyperbolic to elliptical dispersions[9–11]. In contrast to 2D electronic materials, 2D photonic lattices have increased design flexibility for moiré-related phenomena because they can be readily fabricated with arbitrary symmetries and twist angles. Photonic moiré lattices exhibit broadband light trapping[12], enhanced optical chirality[13] and lasing from photonic flatbands[14], and they have been theoretically predicted to support magic-angle-induced light localization[15–17] and hyperbolic plasmons[18].

Because the amplitude of optical modes rapidly decays with distance[19–21], moiré patterns within a single plane result in strong interlattice interactions[14]. Stacking two lattices with subwavelength separations (typically <300 nm) enables interlayer near-field coupling and chiral responses via evanescent fields in the visible regime[17,22]. Therefore, most light-trapping and steering properties have been constrained near the vicinity of the 2D lattice. Interlayer far-field interactions may open more degrees of freedom for manipulating light and benefit multilayer photonic device design[23], remote biological sensing[24] and enhancement of moiré excitons[25]. Although light scattering from gratings along the out-of-plane direction has been associated with the Talbot effect[26], long-range interlayer coupling in moiré structures remains a challenge.

Here we show ultralong-range coupling in 2D photonic moiré architectures. We demonstrate that bilayer plasmonic nanoparticle (NP) square lattices spatially separated by hundreds of micrometres exhibit twist-angle-dependent optical responses. This interlayer coupling over distances exceeding three orders of magnitude of lattice periodicity is mediated by dark surface lattice resonances (SLRs)—hybrid modes whose standing waves are preserved out of plane. To maintain the phase coherence between stacked lattices, we determined that the refractive index along the light path needs to be equal to or greater than that associated with the dark SLR. By combining bilayer NP lattices at different twist angles with liquid gain media, we found that the moiré lattice structures can expand approaches to engineer lasing characteristics since the direction of lasing emission can be tuned in real time by varying the twist angle. Also, we constructed a trilayer moiré NP lattice laser that showed simultaneous coupling between the first and second lattice, first and third lattice, and second and third lattice, which highlights the uniqueness of plasmonic NP lattices for multilayer, far-field interactions.

[1]Department of Chemistry, Northwestern University, Evanston, IL, USA. [2]Graduate Program in Applied Physics, Northwestern University, Evanston, IL, USA. [3]Department of Materials Science and Engineering, Northwestern University, Evanston, IL, USA. ✉e-mail: junguan2021@u.northwestern.edu; todom@northwestern.edu

https://doi.org/10.1038/s41565-023-01320-7

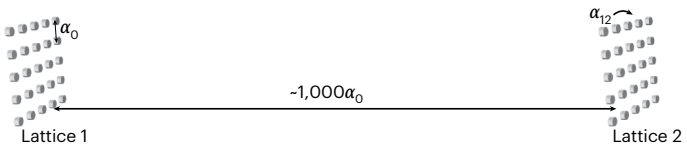

Fig. 1 | Ultralong-range coupling of plasmonic NP lattices in moiré architectures. Here a_0 is the lattice periodicity, 1,000a_0 is the interlayer distance and α_{12} is the twist angle between the first and second lattice.

Long-range coherence from plasmonic NP lattices

Figure 1 depicts the length scales for ultralong-range coupling in moiré photonic lattices. Two identical plasmonic NP lattices (periodicity a_0) can couple to each other even when the lattices are spatially separated by large distances (~1,000a_0). Varying the twist angle α_{12} between the first and second lattice can result in tunable interlayer moiré interactions.

Figure 2a depicts the experimental measurement setup and general construction design to test long-range coherence from a single plasmonic NP lattice. An Al NP lattice (a_0 = 400 nm) fabricated on glass was located at the z position of z_1, and dimethyl sulfoxide (DMSO) was placed above and below the lattice substrate to create similar refractive-index environments. When organic dye molecules were dissolved in DMSO (Fig. 2a, light orange) at $z = z_2$, they functioned as long-range probes to reveal phase coherence far from the lattice at z_1. To identify the photonic modes of the lattice, we first measured the wavelength versus angle optical maps without any dye (Fig. 2b). Because of the slightly different refractive indices of DMSO ($n \approx 1.47$) and glass ($n \approx 1.52$), two sets of diffraction orders from the two index environments were present. The coupling between the (1, 0) and (−1, 0) propagating SLRs at the Γ point (angle, 0°) produces a bright mode via constructive interference at the lower-energy side of the crossing of the optical bands and a dark mode via destructive interference at the higher-energy side[27–29]. These band-edge SLR wavelengths can be approximated by $a_0 \times n$, where n is the refractive index of the solution at z_2. Under plane-wave excitation, dark SLRs can appear at small non-zero angles near the Γ point[28]. Simulated wavelength versus angle maps calculated by the finite-difference time-domain (FDTD) method were in agreement with the measured band structure (Fig. 2c).

To show how the dark SLR modes can preserve phase coherence in the far field from the lattice, we plotted the electric field distributions at the dark SLR wavelength (simulated λ, ~590 nm) at a slight off-normal excitation (incident angle, ~0.5°) (Fig. 2d). We approximated an infinitely thick glass substrate by first calculating the transmitted electromagnetic fields from a periodic Al NP lattice (a_0 = 400 nm) and then importing those fields as the incident light source for the second simulation (Fig. 2d, right) that contains only glass and DMSO. In the NP lattice plane, the electric fields are suppressed at the sites of the NPs from destructive interference and enhanced in areas between the NPs ($|E/E_0|^2 \approx 4$) (Supplementary Fig. 1). Importantly, the periodic intensity distributions are preserved throughout the glass spacer and DMSO, and the electric fields form standing waves that repeat with lattice periodicity in the out-of-plane direction. The real part of the electric field E_y and phase map confirmed

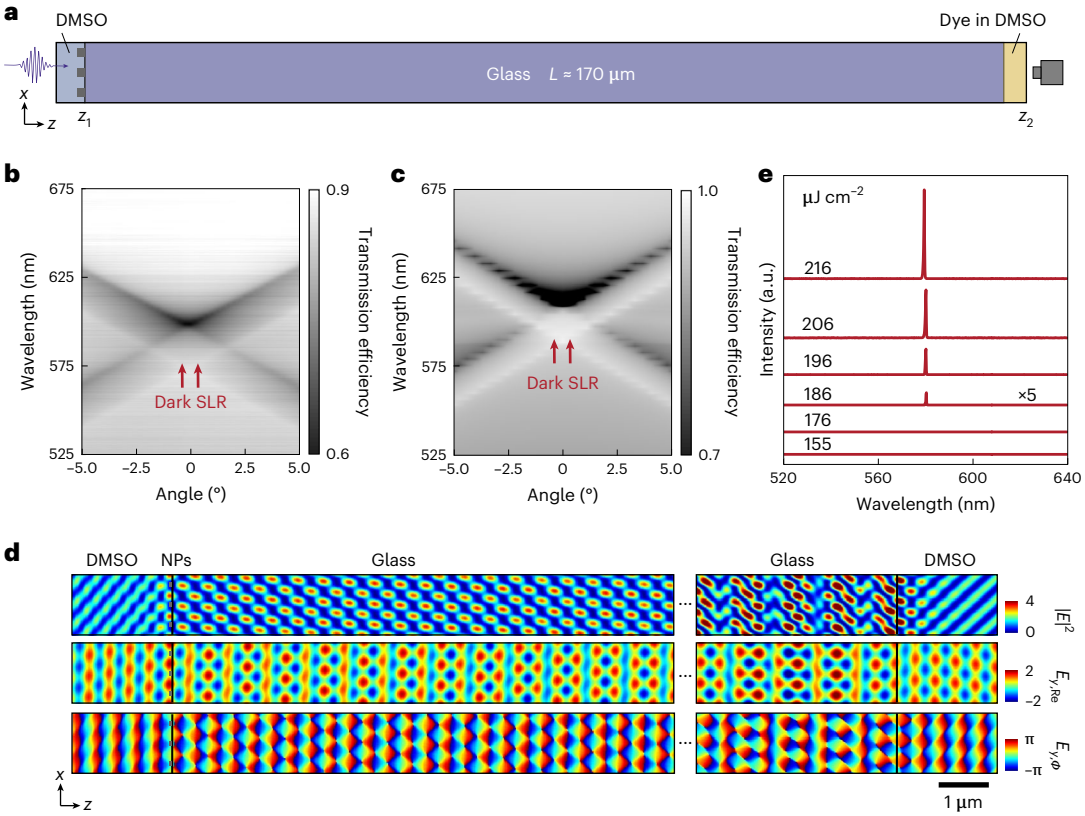

Fig. 2 | Probing ultralong-range phase coherence of dark SLR modes. **a**, Schematic of plasmonic NP lattices (a_0 = 400 nm) where dye molecules are used as local optical probes. The NP diameter d is 90 nm, and NP height h is 50 nm. The lattice is located at z_1 with DMSO as the index-matching solvent; 20 mM C540a–DMSO solution is at z_2. **b**,**c**, Measured (**b**) and simulated (**c**) band structures under transverse-electric polarization show dark SLR modes near the Γ point. The colour bars indicate the value of transmission efficiency. **d**, Simulated electric field distributions indicate ultralong-range phase coherence of the dark SLR mode along the out-of-plane direction. The incident light is transverse-electric polarized along the y direction. The colour bars indicate the electric field $|E|^2$, the real part of E_y ($E_{y,Re}$) and phase of E_y ($E_{y,\phi}$) (from top to bottom). Electric field responses in glass are stronger than those in DMSO because light is more concentrated in higher-refractive-index media. **e**, Measured power-dependent emission spectra of dye molecules at z_2 show lasing above a critical threshold (180 μJ cm^{-2}). The wavelength of the pump laser is 400 nm; the measured dark SLR wavelength is ~580 nm.

https://doi.org/10.1038/s41565-023-01320-7

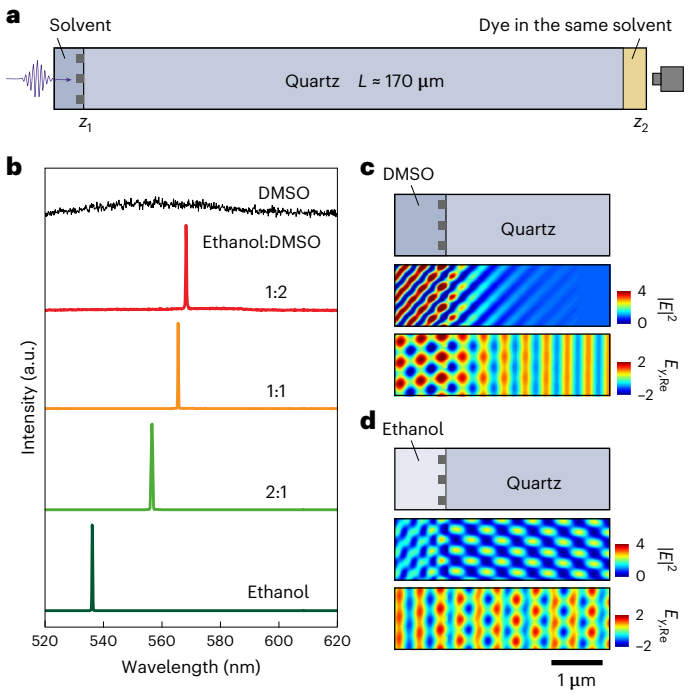

Fig. 3 | Ultralong-range phase coherence of dark SLRs is sensitive to index environment. a, Schematic of lattice design to examine the extent of refractive index on the out-of-plane phase coherence. **b**, Emission spectra of dye molecules in different solvents in **a** indicate that lasing was supported only when $n_{solution} < n_{quartz}$. The lasing spectra were normalized. **c**, With DMSO as the solvent ($n_{DMSO} > n_{quartz}$), the phase coherence gradually disappeared in the quartz spacer. The thickness of quartz was treated as infinite based on the boundary conditions. **d**, With ethanol as the solvent ($n_{ethanol} < n_{quartz}$), phase coherence was preserved in the quartz spacer. The colour bars indicate the electric field $|E|^2$ and the real part of E_y, respectively.

phase coherence at any x–y plane outside the lattice. Without the Al NP lattice, only a propagating-wave pattern was observed (Supplementary Fig. 2). Compared with Al NP lattices, TiO_2 NP lattices with the same NP size showed substantially weaker modulation of the electromagnetic fields and could not support ultralong-range phase coherence (Supplementary Fig. 3).

We used organic dye molecules to probe the dark SLR modes of a single plasmonic NP lattice (Fig. 2a). C540a was chosen because its photoluminescence (PL) spectrally overlaps with the dark SLR near the Γ point of the Al NP lattice ($\lambda \approx 580$ nm). A droplet of C540a–DMSO solution (20 mM) was placed at z_2 with a thickness of ~10 μm and photoexcited by a 400 nm femtosecond pulsed laser (100 Hz) from the z_1 side; the emitted light from the dyes was then transferred to the optical modes in the lattice. The spatially separated dye molecules (at z_2) and the Al NP lattice (at z_1) were only weakly coupled based on the transmission spectrum (Supplementary Fig. 4). Above a critical pump intensity (180 μJ cm^{-2}), a narrow, intense peak above the background emerged ($\lambda \approx 580$ nm; full-width at half-maximum, <0.5 nm) at the dark SLR wavelength (Fig. 2e), which indicates that standing waves in DMSO at z_2 provide optical feedback for lasing. Since lasing was facilitated by the dark SLR mode close to the Γ point, the beam emission was perpendicular to the lattice plane (Supplementary Fig. 5). As a control, we tested the same architecture with TiO_2 NP lattices; however, these dielectric lattices only exhibited PL (Supplementary Figs. 6 and 7). We further confirmed that the lasing emission is not from a Fabry–Pérot (FP) cavity by using a different dye (C500) that spectrally overlaps with the X point of the Al NP lattice (Supplementary Fig. 8), and the lasing wavelength ($\lambda \approx 520$ nm) and emission angle ($\theta \approx 40°$) matched that of the X-point mode.

Waveguide-mediated FP modes could potentially contribute to long-range coupling from either the (1) DMSO/glass spacer/DMSO structure (Supplementary Fig. 9) or (2) air/multilayer/air structure (Supplementary Fig. 10). Simulation results indicate that the hybridization of SLR modes with waveguide-mediated FP modes would introduce numerous FP–SLR modes over a wide range of wavelengths (>20 nm) at the Γ point (Supplementary Figs. 9 and 10). However, these hybrid modes were not observed in the measured band structure, and the lasing signals did not span the full FP–SLR wavelength range; lasing emission only appeared at the dark SLR wavelength and with a narrow linewidth (<0.5 nm). Any internal reflection from the multilayered architecture might enhance coupling from the dark-SLR-mode mechanism and contribute to longer coherence distances and lower lasing thresholds.

Phase coherence sensitive to refractive-index environment

We examined how the refractive-index environment affected the out-of-plane phase coherence using solutions of DMSO and ethanol and quartz substrates ($n \approx 1.45$) for the Al NP lattice (Fig. 3a). Unexpectedly, with DMSO ($n \approx 1.47$) as the solvent for the dye, only PL was observed (Fig. 3b). When ethanol ($n \approx 1.34$) was added to DMSO to lower the solution index at positions z_1 and z_2, lasing was observed when the index of the solution was lower than that of the quartz spacer. As the ethanol:DMSO volume ratio increased, the estimated index of the solution decreased, which shifted the dark SLR modes to shorter wavelengths (Supplementary Fig. 11) as well as the associated lasing wavelengths.

We simulated the electric field distributions in pure solvents, namely, DMSO and ethanol, to understand why the solvent index affected the lasing action. With only DMSO as the solvent around the Al NP lattice on quartz, the simulated dark-SLR-mode wavelength is ~590 nm (Supplementary Fig. 12). Since standing waves from the first simulation are preserved in the second simulation (Fig. 2d), we only considered the electric fields in DMSO–NP–quartz near z_1 to visualize the coherence (Fig. 3c). The periodic features of $|E|^2$ and E_y in the x–y planes along z were preserved in DMSO but gradually disappeared in quartz. In contrast, with ethanol as the solvent, the periodic $|E|^2$ and E_y patterns were maintained in both ethanol and quartz at the dark SLR wavelength (~536 nm) (Fig. 3d). These simulations reveal that phase coherence degrades when light encounters a medium with a lower refractive index than that associated with dark SLR.

The simulated dark SLR wavelength in DMSO spectrally overlaps the range for constructive interference in quartz (>580 nm). Hence, the standing-wave pattern from destructive interference is not preserved and gradually disappears in quartz. In a lower-index solution ($n_{solution} < n_{quartz}$), destructive interference can be maintained (Supplementary Fig. 13), which allows the standing waves to reach the dye region at z_2. Using thicker quartz slides as spacer layers, we determined that the longest phase-coherence distance associated with dark SLR of a 400-nm-square Al NP lattice was 0.5 mm (Supplementary Fig. 14). Moreover, the lasing wavelength does not depend on the index of the spacer (Supplementary Fig. 15), which is different from lasing signals mediated by hybrid waveguide–SLR modes[30–37]. We also tested the robustness of long-range coupling by modulating the refractive index of the spacer layer (Supplementary Fig. 16), and the coherence appears to be tolerant to perturbations.

Tunable moiré lasing from macroscale-separated lattices

Figure 4a depicts a bilayer moiré architecture with large spatial separation ($L \approx 170$ μm) that can support ultralong-range coupling between two lattices. The first lattice was fixed on the edge of a sample holder,

https://doi.org/10.1038/s41565-023-01320-7

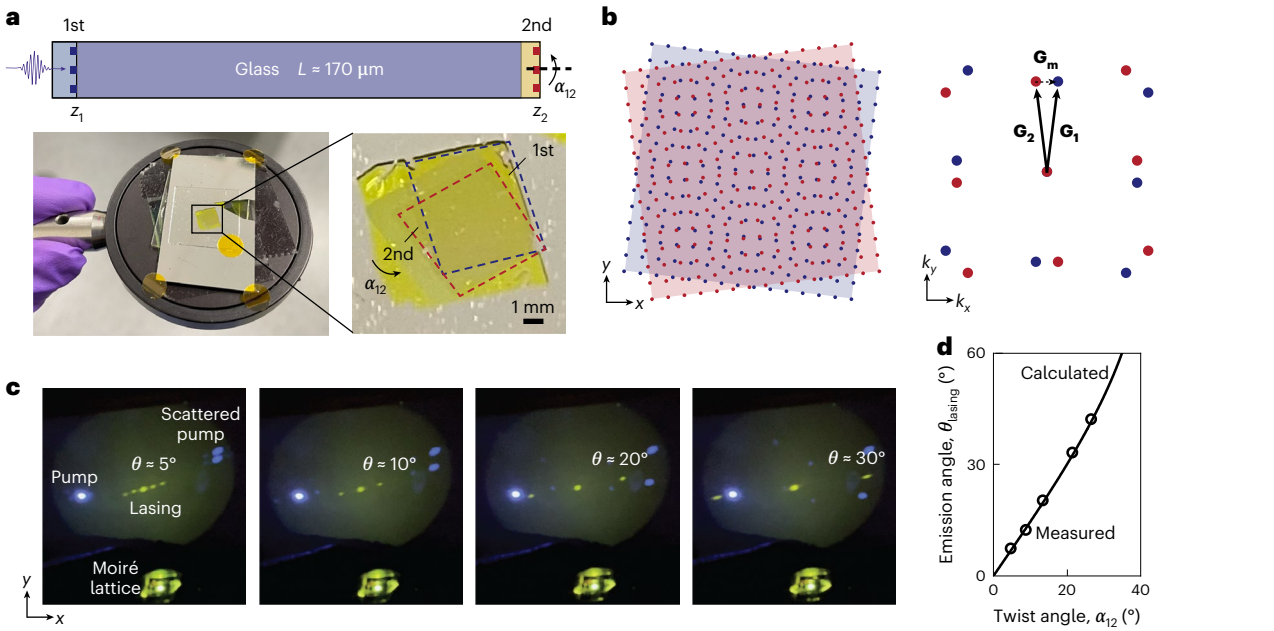

Fig. 4 | Tunable moiré lasers from macroscale-separated NP lattices. **a**, Schematic of a bilayer moiré lattice and optical micrographs of the fabricated bilayer structures. Two Al NP lattices with the same periodicity (a_0 = 400 nm) and particle dimensions (d = 90 nm, h = 50 nm) were prepared on two different glass substrates. The first lattice at z_1 was combined with DMSO. The second lattice at z_2 was surrounded with 20 mM C540a–DMSO solution. Here α_{12} is the twist angle between the first and second lattice. **b**, Real space (left) and reciprocal space (right) of the overlayed lattices. Each colour (red or blue) represents one lattice. Here $\mathbf{G_1}$ and $\mathbf{G_2}$ are the reciprocal lattice vectors of the two lattices and $\mathbf{G_m}$ is the moiré reciprocal vector, defined as $\mathbf{G_m} = \mathbf{G_1} + \mathbf{G_2}$. **c**, Real-time tunable lasing emission angles by varying the lattice twist angle. The blue beams are the pump beams. The yellow spots are the lasing beams captured on a white piece of paper. θ is the moiré lasing angle. **d**, Measured emission angle (θ_{lasing}) versus twist angle (α_{12}) relation agrees with the calculated empty moiré lattice dispersion.

whereas the second lattice was mounted on the inner part of a holder that can be manually rotated over 360°. To determine the twist angle between the first and second lattice (α_{12}), we evaluated the moiré structure captured in an optical image to identify the relative angle between the patterned areas. Because the NP lattices and their substrates were separated by a DMSO liquid layer, the twist angle could be tuned in real time via rotation of the first lattice.

Because of the ultralong phase coherence of dark SLRs, the periodic electric field distributions from the first lattice can extend to the plane of the second lattice, where the two dark SLR modes can effectively couple in the same plane. To understand the far-field interlayer interactions, we plotted the real space and reciprocal space of the overlapped lattices (Fig. 4b). The empty-lattice dispersion relation of a moiré lattice can be described as $|\mathbf{k}_{\parallel} + \mathbf{G_1} + \mathbf{G_2}| = n\frac{E}{\hbar c}$, where $\mathbf{k}_{\parallel}$ is the wavevector component parallel to the lattice plane; $\mathbf{G_1}$ and $\mathbf{G_2}$ are the reciprocal lattice vectors of the first and second lattice, respectively; n is the refractive index; E is the photon energy; $\hbar$ is the Planck constant; c is the speed of light in vacuum; and the moiré reciprocal vectors are defined as $\mathbf{G_m} = \mathbf{G_1} + \mathbf{G_2}$. From the conservation of crystal momentum[38], the band-edge states at $\mathbf{k}_{\parallel} = 0$ will also appear at $\mathbf{k}_{\parallel} = \mathbf{G_m}$ (Supplementary Fig. 17); therefore, $\mathbf{G_m}$ can be used to evaluate the off-normal band-edge states. A smaller twist angle (α_{12}) results in smaller $|\mathbf{G_m}|$ in reciprocal space, which corresponds to moiré modes at smaller emission angles normal to the NP lattice (θ_{lasing}). Based on the geometry of the triangle formed by $\mathbf{G_1}$, $\mathbf{G_2}$ and $\mathbf{G_m}$, the relation between α_{12} and θ_{lasing} can be expressed as $\sin\theta_{lasing} = n\sqrt{2 - 2\cos\alpha_{12}}$.

To investigate moiré phenomena in ultralong-range coupled lattices, we optically pumped the bilayer device using 400 nm, 100 fs pulses (spot size, ~1 mm) from the z_1 side (Fig. 4a). Above a critical threshold, we observed multiple lasing beams in the far field, which indicates that the projected moiré modes provide optical feedback (Fig. 4c). We demonstrated real-time tunable lasing emission over a wide angular range (θ_{lasing} = 0–45°) by rotating the first lattice (α_{12} = 0–30°); increasing the twist angle α_{12} resulted in lasing beams emitted at higher angles (Supplementary Video 1). The lasing beams were observed only along a single lattice direction because only dye molecules with transition dipole moments along the pump polarization (x direction) are excited[39,40] and coupled to the moiré modes along x.

By plotting the emission angle versus twist angle, we showed that the measured angles quantitatively agree with the calculated values (Fig. 4d and Supplementary Fig. 18). Emission angles were collected only up to $\theta_{lasing} \approx 45°$ because the edge of the sample holder blocks lasing beams emitted at larger angles (>45°). Since an incommensurate lattice can be approximated as a commensurate lattice of a finite area[41], the ultralong-range coupled moiré laser device is tolerant to small variations in twist angle. The moiré lattice laser is also robust against translational mismatch because the off-normal band edges are determined by moiré periodicity, which is not affected by translational variation. We note that the off-normal moiré band edges could not be resolved in the measured optical dispersion diagram (Supplementary Fig. 19) and only indirectly identified by the lasing signals; lasing has been shown to be a sensitive probe of optical modes[30,31,42–52]. If the symmetry of the symmetric square lattice is reduced in either of the NP lattices, we expect that additional lasing wavelengths and emission angles will be determined by the projected moiré superlattice when additional dark SLRs spectrally overlap with the PL of the gain.

Trilayer moiré effects from macroscale-separated lattices

We constructed a three-layer moiré structure to demonstrate that ultralong-range coupling is supported among multilayer lattices (Fig. 5a). Since coupling among three lattices can introduce a large number of moiré photonic modes at various emission angles (θ_{lasing}), for simplicity, we fixed the relative twist angles of the three lattices with high mirror symmetry (Fig. 5b). The twist angles were optimized at $\alpha_{13} = \alpha_{23} = \alpha_{12}/2 = 12°$, which guaranteed that the multiple off-normal

https://doi.org/10.1038/s41565-023-01320-7

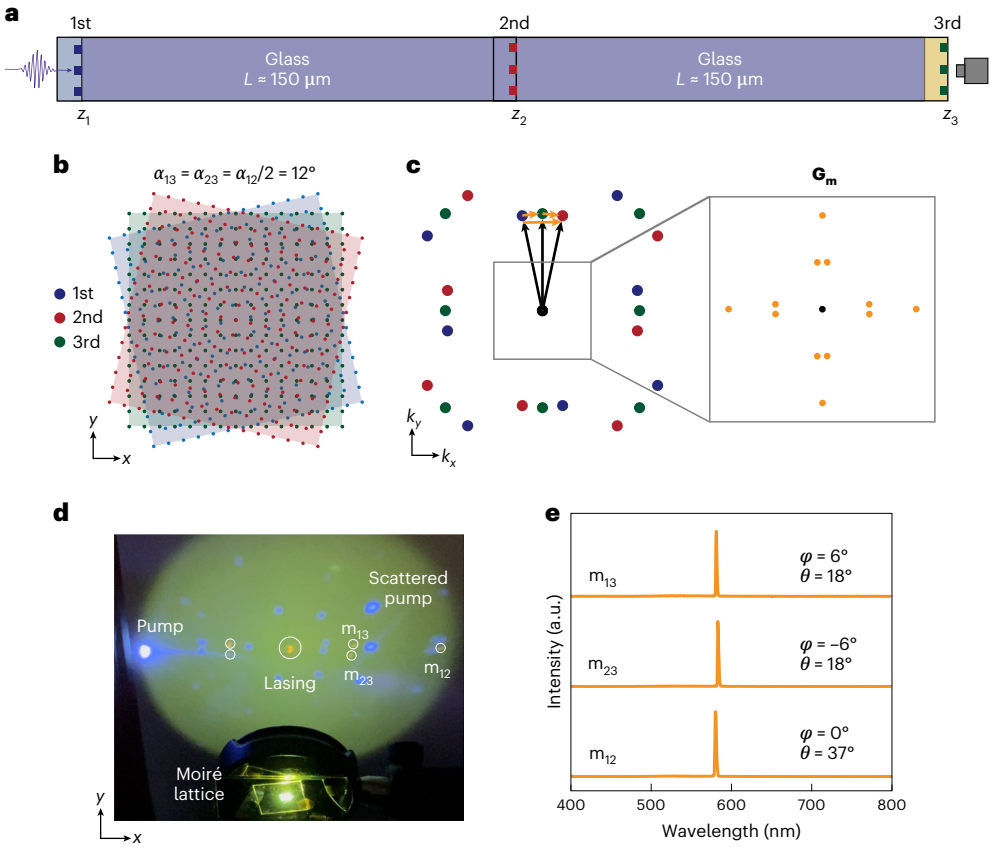

Fig. 5 | Three-layer moiré effect from macroscale-separated NP lattices. **a**, Schematic of three-layer moiré lattices (a_0 = 400 nm, d = 90 nm, h = 50 nm). The first, second and third lattice are at z_1, z_2 and z_3, respectively. DMSO and oil ($n \approx 1.52$) were used as the index-matching solvents for the first and second lattice, respectively, and 20 mM C540a–DMSO solution was integrated with the third lattice. **b**, Real space of the three-layer moiré lattice. Blue, red and green dots represent the first, second and third lattice, respectively. **c**, Reciprocal space of moiré lattice and the moiré reciprocal vector $\mathbf{G_m}$. The black arrows represent the reciprocal vectors $\mathbf{G_1}$, $\mathbf{G_2}$ and $\mathbf{G_3}$ of the corresponding individual lattices. The orange arrows represent the moiré reciprocal vectors $\mathbf{G_m}$ from the coupling among the three lattices, and $\mathbf{G_m}$ values are also plotted in k-space as orange dots. **d**, Photograph of the emission beams showed off-normal lasing resulting from three-layer coupling. θ and ϕ are the polar and azimuthal angles of the moiré lasing beams (orange spots), respectively. **e**, Measured lasing emission angles agree with the calculations. The lasing spectra were normalized.

emission beams were separated for far-field measurements. The transmission spectrum of the three-layer structure showed a dark SLR mode at ~580 nm, which is close to the dark SLR wavelength in DMSO (Supplementary Fig. 20). The empty-lattice dispersion relation of a three-layer moiré lattice is described as $|\mathbf{k}_{\parallel} + \mathbf{G_1} + \mathbf{G_2} + \mathbf{G_3}| = n\frac{E}{\hbar c}$, where $\mathbf{G_1}$, $\mathbf{G_2}$ and $\mathbf{G_3}$ are the reciprocal lattice vectors of the first, second and third lattice, respectively. Since the moiré reciprocal vectors $\mathbf{G_m} = \mathbf{G_1} + \mathbf{G_2} + \mathbf{G_3}$ can represent the in-plane wavevectors of off-normal moiré modes, we plotted the smallest non-zero $\mathbf{G_m}$ as orange points in k space to represent the moiré modes (Fig. 5c). The $\mathbf{G_m}$ vectors can be converted to moiré lasing emission angles using the relation $\sin\theta_{ij} = n\sqrt{2 - 2\cos\alpha_{ij}}$, where $i, j = 1, 2, 3$ and $i \neq j$. The predicted off-normal emission angles are at (θ_{lasing}, φ_{lasing}) = (18°, ±6°/±84°/±96°/±174°) and (37°, 0°/90°/180°/270°).

To experimentally verify the ultralong-range coupling among three NP lattices, we photoexcited dye molecules in DMSO at z_3 from the z_1 side and captured the lasing signals on the z_3 side (Fig. 5d). We observed one lasing spot at $\theta_{\text{lasing}} \approx 0°$ that can be associated with dark SLRs near the Γ point from any of the three individual square lattices. Six moiré lasing spots appeared on the sides, where the m_{13} beam arises from the coupling between the first and third lattice; the m_{23} beam, coupling between the second and third lattice; and the m_{12} beam, coupling between the first and second lattice. We identified the moiré lasing angles by rotating the fibre detector and the three-layer device (Fig. 5e and Supplementary Fig. 21). Because of the mirror symmetry of the stacked lattices, m_{13} and m_{23} were at the same emission angle (θ_{lasing}) but at different azimuthal angles (φ_{lasing}). The measured lasing emission angles agree with the locations of the calculated moiré modes, which demonstrates simultaneous coupling among the three lattices. Our observation also confirmed that the spatially separated multilayer NP lattices can be evaluated based on their 2D projection and that moiré lasing properties match well with that predicted using the empty-lattice approximation, indicating that the waveguide effects are not needed to interpret the mechanism.

Conclusion

In summary, we have demonstrated far-field coupling between photonic lattices in bilayer and trilayer moiré architectures. This work provides a critical insight into how plasmonic NP lattices can maintain phase coherence far from the lattice plane, which enables the vertical dimension of a 2D lattice to function as an additional degree of freedom for controlling light–matter interactions. For example, dark modes in 2D NP lattices offer design prospects for organic and quantum dot light-emitting diodes, where NP lattices can be added to any layer far from the emissive materials to enhance the output efficiencies. Also, a strong coupling between the molecules and NP lattices may result in long-range exciton polaritons. Tuning coupled optical modes in bilayer lattices may enable devices that exhibit non-Hermitian physics,

where a balance between gain and loss could lead to unidirectional light transport. We anticipate that these extended interactions across lattices will open diverse applications in reconfigurable photonic systems, biosensors and nano-optics.

Online content

Any methods, additional references, Nature Portfolio reporting summaries, source data, extended data, supplementary information, acknowledgements, peer review information; details of author contributions and competing interests; and statements of data and code availability are available at https://doi.org/10.1038/s41565-023-01320-7.

References

1. Andrei, E. Y. & MacDonald, A. H. Graphene bilayers with a twist. *Nat. Mater.* **19**, 1265–1275 (2020).
2. Andrei, E. Y. et al. The marvels of moiré materials. *Nat. Rev. Mater.* **6**, 201–206 (2021).
3. Mak, K. F. & Shan, J. Semiconductor moiré materials. *Nat. Nanotechnol.* **17**, 686–695 (2022).
4. Cao, Y. et al. Unconventional superconductivity in magic-angle graphene superlattices. *Nature* **556**, 43–50 (2018).
5. Cao, Y. et al. Correlated insulator behaviour at half-filling in magic-angle graphene superlattices. *Nature* **556**, 80–84 (2018).
6. Yankowitz, M. et al. Tuning superconductivity in twisted bilayer graphene. *Science* **363**, 1059–1064 (2019).
7. Serlin, M. et al. Intrinsic quantized anomalous Hall effect in a moiré heterostructure. *Science* **367**, 900–903 (2020).
8. Sharpe, A. L. et al. Emergent ferromagnetism near three-quarters filling in twisted bilayer graphene. *Science* **365**, 605–608 (2019).
9. Hu, G. W. et al. Topological polaritons and photonic magic angles in twisted α-MoO_3 bilayers. *Nature* **582**, 209–213 (2020).
10. Chen, M. et al. Configurable phonon polaritons in twisted α-MoO_3. *Nat. Mater.* **19**, 1307–1311 (2020).
11. Duan, J. et al. Twisted nano-optics: manipulating light at the nanoscale with twisted phonon polaritonic slabs. *Nano Lett.* **20**, 5323–5329 (2020).
12. Lubin, S. M., Zhou, W., Hryn, A. J., Huntington, M. D. & Odom, T. W. High-rotational symmetry lattices fabricated by moiré nanolithography. *Nano Lett.* **12**, 4948–4952 (2012).
13. Wu, Z. L. & Zheng, Y. B. Moiré metamaterials and metasurfaces. *Adv. Opt. Mater.* **6**, 1701057 (2018).
14. Mao, X. R., Shao, Z. K., Luan, H. Y., Wang, S. L. & Ma, R. M. Magic-angle lasers in nanostructured moiré superlattice. *Nat. Nanotechnol.* **16**, 1099–1105 (2021).
15. Tang, H. N. et al. Modeling the optical properties of twisted bilayer photonic crystals. *Light Sci. Appl.* **10**, 157 (2021).
16. Dong, K. C. et al. Flat bands in magic-angle bilayer photonic crystals at small twists. *Phys. Rev. Lett.* **126**, 223601 (2021).
17. Lou, B. C. et al. Theory for twisted bilayer photonic crystal slabs. *Phys. Rev. Lett.* **126**, 136101 (2021).
18. Hu, G., Krasnok, A., Mazor, Y., Qiu, C.-W. & Alù, A. Moiré hyperbolic metasurfaces. *Nano Lett.* **20**, 3217–3224 (2020).
19. Adams, M. J. *An Introduction to Optical Waveguides* (John Wiley & Sons, 1981).
20. Hutter, E. & Fendler, J. H. Exploitation of localized surface plasmon resonance. *Adv. Mater.* **16**, 1685–1706 (2004).
21. Haes, A. J., Zou, S., Schatz, G. C. & Van Duyne, R. P. A nanoscale optical biosensor: the long-range distance dependence of the localized surface plasmon resonance of noble metal nanoparticles. *J. Phys. Chem. B* **108**, 109–116 (2004).
22. Wu, Z. L. & Zheng, Y. B. Moiré chiral metamaterials. *Adv. Opt. Mater.* **5**, 1700034 (2017).
23. Vardeny, Z. V., Nahata, A. & Agrawal, A. Optics of photonic quasicrystals. *Nat. Photon.* **7**, 177–187 (2013).
24. Li, Z. P., Tian, X., Qiu, C. W. & Ho, J. S. Metasurfaces for bioelectronics and healthcare. *Nat. Electron.* **4**, 382–391 (2021).
25. Regan, E. C. et al. Emerging exciton physics in transition metal dichalcogenide heterobilayers. *Nat. Rev. Mater.* **7**, 778–795 (2022).
26. Wen, J. M., Zhang, Y. & Xiao, M. The Talbot effect: recent advances in classical optics, nonlinear optics, and quantum optics. *Adv. Opt. Photon.* **5**, 83–130 (2013).
27. Hakala, T. K. et al. Lasing in dark and bright modes of a finite-sized plasmonic lattice. *Nat. Commun.* **8**, 13687 (2017).
28. Rodriguez, S. R. K. et al. Coupling bright and dark plasmonic lattice resonances. *Phys. Rev. X* **1**, 021019 (2011).
29. Heilmann, R., Salerno, G., Cuerda, J., Hakala, T. K. & Torma, P. Quasi-BIC mode lasing in a quadrumer plasmonic lattice. *ACS Photon.* **9**, 224–232 (2022).
30. Guan, J. et al. Quantum dot-plasmon lasing with controlled polarization patterns. *ACS Nano* **14**, 3426–3433 (2020).
31. Guan, J. et al. Engineering directionality in quantum dot shell lasing using plasmonic lattices. *Nano Lett.* **20**, 1468–1474 (2020).
32. Watkins, N. E. et al. Surface normal lasing from CdSe nanoplatelets coupled to aluminum plasmonic nanoparticle lattices. *J. Phys. Chem. C* **125**, 19874–19879 (2021).
33. Tan, M. J. et al. Lasing action from quasi-propagating modes. *Adv. Mater.* **34**, 2203999 (2022).
34. Winkler, J. M. et al. Dual-wavelength lasing in quantum-dot plasmonic lattice lasers. *ACS Nano* **14**, 5223–5232 (2020).
35. Park, J.-E. et al. Polariton dynamics in two-dimensional Ruddlesden–Popper perovskites strongly coupled with plasmonic lattices. *ACS Nano* **16**, 3917–3925 (2022).
36. Schokker, A. H. & Koenderink, A. F. Lasing at the band edges of plasmonic lattices. *Phys. Rev. B* **90**, 155452 (2014).
37. Schokker, A. H., van Riggelen, F., Hadad, Y., Alù, A. & Koenderink, A. F. Systematic study of the hybrid plasmonic-photonic band structure underlying lasing action of diffractive plasmon particle lattices. *Phys. Rev. B* **95**, 085409 (2017).
38. Ashcroft, N. W. & Mermin, N. D. *Solid State Physics* (Cengage Learning, 2011).
39. Schäfer, F. P. *Dye Lasers* (Springer Science & Business Media, 2013).
40. Wang, D. et al. Band-edge engineering for controlled multi-modal nanolasing in plasmonic superlattices. *Nat. Nanotechnol.* **12**, 889–894 (2017).
41. Wang, P. et al. Localization and delocalization of light in photonic moiré lattices. *Nature* **577**, 42–46 (2020).
42. Guan, J. et al. Identification of Brillouin zones by in-plane lasing from light-cone surface lattice resonances. *ACS Nano* **15**, 5567–5573 (2021).
43. Li, R. et al. Hierarchical hybridization in plasmonic honeycomb lattices. *Nano Lett.* **19**, 6435–6441 (2019).
44. Juarez, X. G. et al. *M*-point lasing in hexagonal and honeycomb plasmonic lattices. *ACS Photon.* **9**, 52–58 (2022).
45. Fernandez-Bravo, A. et al. Ultralow-threshold, continuous-wave upconverting lasing from subwavelength plasmons. *Nat. Mater.* **18**, 1172–1176 (2019).
46. Guan, J. et al. Plasmonic nanoparticle lattice devices for white-light lasing. *Adv. Mater.* 2103262 (2021).
47. Lin, Y. H. et al. Engineering symmetry-breaking nanocrescent arrays for nanolasing. *Adv. Funct. Mater.* **29**, 1904157 (2019).
48. Deng, S. K. et al. Ultranarrow plasmon resonances from annealed nanoparticle lattices. *Proc. Natl Acad. Sci. USA* **117**, 23380–23384 (2020).

49. Guo, R., Nečada, M., Hakala, T. K., Väkeväinen, A. I. & Törmä, P. Lasing at *k*-points of a honeycomb plasmonic lattice. *Phys. Rev. Lett.* **122**, 013901 (2019).
50. Daskalakis, K. S., Vakevainen, A. I., Martikainen, J. P., Hakala, T. K. & Torma, P. Ultrafast pulse generation in an organic nanoparticle-array laser. *Nano Lett.* **18**, 2658–2665 (2018).
51. Rekola, H. T., Hakala, T. K. & Torma, P. One-dimensional plasmonic nanoparticle chain lasers. *ACS Photon.* **5**, 1822–1826 (2018).
52. Guan, J. et al. Light-matter interactions in hybrid material metasurfaces. *Chem. Rev.* **122**, 15177–15203 (2022).

Methods

Fabrication of Al NP lattices

Al NP lattices were fabricated using a soft nanofabrication process[53,54]. First, periodic photoresist posts were generated on Si wafers by solvent-assisted nanoscale embossing (SANE) (ref. [55]). Next, 8 nm Cr was deposited on the Si substrate by thermal evaporation followed by the removal of photoresist posts. After deep reactive ion etching to create cylindrical Si pits beneath the circular holes in the Cr film (depth, ~200 nm), the deposition of 100 nm Au produced a Au hole film. Wet etching of the Cr sacrificial layer released the Au hole film from the Si, and then the Au hole film could be used as a deposition mask to create plasmonic NP lattices (area, ~0.5 cm^2) on transparent substrates. Al deposition via electron-beam evaporation through the Au hole mask and then removal of the Au mask with an adhesive tape resulted in Al NP lattices on glass or quartz substrates.

FDTD simulations

The linear optical properties of Al NP lattices were simulated by FDTD calculations using commercial software (FDTD Solutions, Lumerical). In the *x* and *y* directions, Bloch boundary conditions were applied to simulate infinite lattices. In the *z* direction, boundary conditions with perfectly matched layers were used to absorb the light waves. The optical constants of Al were taken from Palik measurements[56]. The glass, quartz and dye solvents (DMSO and ethanol) were simulated by a dielectric model where the material has a specified index at all the frequencies. A uniform mesh size of 4 nm (*x*, *y* and *z* directions) surrounding the Al NPs ensures the accurate calculations of electromagnetic fields.

Lasing measurements

Samples were mounted on a rotational holder so that the angle of the lattice relative to the detector could be controlled. Dyes were optically pumped using 100 fs, 400 nm laser pulses with a repetition rate of 100 Hz; the circular pump spot size was ~1 mm in diameter. The 400 nm laser pulses were generated by directing the 800 nm output from a Ti:sapphire laser into a beta-barium borate crystal to produce the doubled frequency of 400 nm. The pump energy was controlled using a variable neutral density filter. Far-field emission spectra were captured using a charge-coupled device spectrometer (LN2-cooled charge-coupled device/Triax 552, Horiba Jobin Yvon; resolution, ~0.2 nm) or a compact spectrometer (USB 2000, Ocean Optics; resolution, ~1 nm). The details of the optical setup are described in previously published work[40,42,46].

Data availability

Source data are provided with this paper. All other data that support the plots within this paper and other findings of this study are available from the corresponding authors upon reasonable request.

References

53. Henzie, J., Kwak, E. S. & Odom, T. W. Mesoscale metallic pyramids with nanoscale tips. *Nano Lett.* **5**, 1199–1202 (2005).
54. Gao, H., Henzie, J. & Odom, T. W. Direct evidence for surface plasmon-mediated enhanced light transmission through metallic nanohole arrays. *Nano Lett.* **6**, 2104–2108 (2006).
55. Lee, M. H., Huntington, M. D., Zhou, W., Yang, J.-C. & Odom, T. W. Programmable soft lithography: solvent-assisted nanoscale embossing. *Nano Lett.* **11**, 311–315 (2011).
56. Johnson, P. B. & Christy, R.-W. Optical constants of the noble metals. *Phys. Rev. B* **6**, 4370 (1972).

Acknowledgements

This work was supported by the National Science Foundation (NSF) under DMR-1904385 (dyes as dipole sources; J.H., Y.W., M.J.H.T., G.C.S. and T.W.O.), DMR-2207215 (stacked nanoparticle lattice design; J.G., G.C.S. and T.W.O.) and CMMI-2028773 (in-plane moiré lattice model; T.W.O.). This work used the Northwestern University Micro/Nano Fabrication Facility (NUFAB), which is partially supported by Soft and Hybrid Nanotechnology Experimental (SHyNE) Resource (NSF ECCS-2025633), the Materials Research Science and Engineering Center (MRSEC) (DMR-1720139), the State of Illinois and Northwestern University. This work made use of the EPIC facilities of Northwestern University's NUANCE Center, which received support from the SHyNE Resource (NSF ECCS-2025633); the MRSEC program (NSF DMR-1720139) at the Materials Research Center; the International Institute for Nanotechnology (IIN); the Keck Foundation; and the State of Illinois through the IIN. This research was supported in part by the Quest high-performance computing facility at Northwestern University, which is jointly supported by the Office of the Provost, the Office for Research and Northwestern University Information Technology.

Author contributions

J.G. and T.W.O. conceived the idea of moiré photonic lattices. J.G. and J.H. designed the moiré architecture, fabricated the plasmonic NP lattices, characterized the linear optical properties of the devices and performed the FDTD numerical simulations. J.G., J.H., Y.W. and M.J.H.T. carried out the lasing measurements. Y.W. fabricated the TiO_2 NP lattices. G.C.S. guided the theoretical investigations. J.G. and T.W.O. analysed the data and wrote the manuscript. All the authors commented on and revised the manuscript.

Competing interests

The authors declare no competing interests.

Additional information

Supplementary information The online version contains supplementary material available at https://doi.org/10.1038/s41565-023-01320-7.

Correspondence and requests for materials should be addressed to Jun Guan or Teri W. Odom.

Peer review information *Nature Nanotechnology* thanks Fangwei Ye and the other, anonymous, reviewer(s) for their contribution to the peer review of this work.